Mutations in *ARMC9*, which Encodes a Basal Body Protein, Cause Joubert Syndrome in Humans and Ciliopathy Phenotypes in Zebrafish

Julie C. Van De Weghe,[1,16] Tamara D.S. Rusterholz,[2,16] Brooke Latour,[3,4,16] Megan E. Grout,[1] Kimberly A. Aldinger,[1,5] Ranad Shaheen,[6] Jennifer C. Dempsey,[1] Sateesh Maddirevula,[6] Yong-Han H. Cheng,[1] Ian G. Phelps,[1] Matthias Gesemann,[2] Himanshu Goel,[7,8] Ohad S. Birk,[9] Talal Alanzi,[6] Rifaat Rawashdeh,[6] Arif O. Khan,[6,10] University of Washington Center for Mendelian Genomics, Michael J. Bamshad,[1,11] Deborah A. Nickerson,[11] Stephan C.F. Neuhauss,[2] William B. Dobyns,[1,5,12] Fowzan S. Alkuraya,[6,13,14] Ronald Roepman,[3,4,16] Ruxandra Bachmann-Gagescu,[2,15,16,*] and Dan Doherty[1,5,16,*]

Joubert syndrome (JS) is a recessive neurodevelopmental disorder characterized by hypotonia, ataxia, abnormal eye movements, and variable cognitive impairment. It is defined by a distinctive brain malformation known as the “molar tooth sign” on axial MRI. Subsets of affected individuals have malformations such as coloboma, polydactyly, and encephalocele, as well as progressive retinal dystrophy, fibrocystic kidney disease, and liver fibrosis. More than 35 genes have been associated with JS, but in a subset of families the genetic cause remains unknown. All of the gene products localize in and around the primary cilium, making JS a canonical ciliopathy. Ciliopathies are unified by their overlapping clinical features and underlying mechanisms involving ciliary dysfunction. In this work, we identify biallelic rare, predicted-deleterious *ARMC9* variants (stop-gain, missense, splice-site, and single-exon deletion) in 11 individuals with JS from 8 families, accounting for approximately 1% of the disorder. The associated phenotypes range from isolated neurological involvement to JS with retinal dystrophy, additional brain abnormalities (e.g., heterotopia, Dandy-Walker malformation), pituitary insufficiency, and/or synpolydactyly. We show that ARMC9 localizes to the basal body of the cilium and is upregulated during ciliogenesis. Typical ciliopathy phenotypes (curved body shape, retinal dystrophy, coloboma, and decreased cilia) in a CRISPR/Cas9-engineered zebrafish mutant model provide additional support for *ARMC9* as a ciliopathy-associated gene. Identifying *ARMC9* mutations as a cause of JS takes us one step closer to a full genetic understanding of this important disorder and enables future functional work to define the central biological mechanisms underlying JS and other ciliopathies.

Introduction

Joubert syndrome (JS [MIM: P213330]) is a recessive neurodevelopmental disorder characterized by motor and cognitive impairments and a distinctive hindbrain malformation giving the appearance of the “molar tooth sign” (MTS) on axial MRI. In addition to the obligate neurological features, subsets of individuals with JS have progressive retinal dystrophy, fibrocystic kidney disease, and liver fibrosis, as well as malformations such as chorioretinal coloboma and polydactyly. Despite this distinctive clinical presentation, mutations in more than 35 genes cause JS, highlighting its marked genetic heterogeneity.[1–24] All of the genes to date encode proteins that function in or around the primary cilium, rendering JS a canonical ciliopathy; ciliopathies are disorders grouped by their overlapping clinical features and molecular disease mechanisms involving cilium dysfunction.[24–27] The primary cilium is a nearly ubiquitous microtubule-based organelle sheathed in a specialized membrane that projects from the cellular surface and functions like an antenna, detecting light, mechanical, and chemical cues, as well as regulating key signaling pathways such as Hedgehog[28–34] and PDGF.[35,36] Significant advances have been made in recent years on the complex genetics underlying JS, and multiple cellular and developmental defects have been associated with loss of function for JS-associated genes in model systems.[11,22,31,37–45] Despite this remarkable progress identifying candidate mechanisms, the common cellular dysfunction across genetic causes of JS is elusive. Therefore it is essential to identify the complete set of genetic defects that underlie JS to pinpoint the unifying molecular

[1] Department of Pediatrics, University of Washington, Seattle, WA 98195, USA; [2] Institute of Molecular Life Sciences, University of Zurich, 8057 Zurich, Switzerland; [3] Department of Human Genetics, Radboud University Medical Center, 6500 HB Nijmegen, the Netherlands; [4] Radboud Institute for Molecular Life Sciences, Radboud University Medical Center, 6525 GA Nijmegen, the Netherlands; [5] Center for Integrative Brain Research, Seattle Children’s Research Institute, Seattle, WA 98101, USA; [6] Department of Genetics, King Faisal Specialist Hospital and Research Center, Riyadh 12713, Saudi Arabia; [7] Hunter Genetics, Waratah, NSW 2298, Australia; [8] University of Newcastle, Callaghan, NSW 2308, Australia; [9] Genetics Institute, Soroka Medical Center and National Institute for Biotechnology in the Negev (NIBN), Ben Gurion University, Beer Sheva 8499000, Israel; [10] Eye Institute, Cleveland Clinic Abu Dhabi, Abu Dhabi, United Arab Emirates; [11] Department of Genome Sciences, University of Washington, Seattle, WA 98195, USA; [12] Department of Neurology, University of Washington, Seattle, WA 98195, USA; [13] Department of Anatomy and Cell Biology, College of Medicine, Alfaisal University, Riyadh 11533, Saudi Arabia; [14] Saudi Human Genome Program, King Abdulaziz City for Science and Technology, Riyadh 12371, Saudi Arabia; [15] Institute of Medical Genetics, University of Zurich, 8952 Schlieren, Switzerland

[16] These authors contributed equally to this work

*Correspondence: ruxandra.bachmann@imls.uzh.ch (R.B.-G.), ddoher@uw.edu (D.D.)

http://dx.doi.org/10.1016/j.ajhg.2017.05.010.

mechanism. In this work, we present evidence for mutations in armadillo repeat containing 9 (*ARMC9*) as a cause of JS, based on human genetic, protein localization, and zebrafish model data.

Material and Methods

Subject Ascertainment and Phenotypic Data

Informed consent was obtained for all participants, who were enrolled under approved human subjects research protocols at the University of Washington (UW), Seattle Children's Hospital, or King Faisal Specialist Hospital and Research Centre (KFSHRC). All participants have clinical findings of JS (intellectual impairment, hypotonia, ataxia, and/or oculomotor apraxia) and diagnostic or supportive brain imaging findings (MTS or cerebellar vermis hypoplasia). Clinical data were obtained by direct examination of participants, review of medical records, and structured questionnaires.

Variant Identification

Samples from individuals affected by JS were previously screened using a molecular inversion probes (MIPs) targeted capture[46] for *AHI1* (MIM: 608894), *ARL13B* (MIM: 608922), *B9D1* (MIM: 614144), *B9D2* (MIM: 611951), *C2CD3* (MIM: 615944), *C5ORF42* (MIM: 614571), *CC2D2A* (MIM: 612013), *CEP290* (MIM: 61042), *CEP41* (MIM: 610523), *CSPP1* (MIM: 611654), *IFT172* (MIM: 607386), *INPP5E* (MIM: 613037), *KIF7* (MIM: 611254), *MKS1* (MIM: 609883), *NPHP1* (MIM: 607100), *OFD1* (MIM: 300170), *RPGRIP1L* (MIM: 610937), *TCTN1* (MIM: 609863), *TCTN2* (MIM: 613846), *TCTN3* (MIM: 613847), *TMEM138* (MIM: 614459), *TMEM216* (MIM: 613277), *TMEM231* (MIM: 614949), *TMEM237* (MIM: 614423), *TMEM67* (MIM: 609884), *TTC21B* (MIM: 612014), and *ZNF423* (MIM: 604557).[1–24,47] In samples without causal variants, exome sequencing was performed as previously described[48] using Roche Nimblegen SeqCap EZ Human Exome Library v2.0 capture probes (36.5 Mb of coding exons) and paired-end 50 base pair reads on an Illumina HiSeq sequencer. In accordance with the Genome Analysis ToolKit's (GATK) best practices, we mapped sequence reads to the human reference genome (hg19) using the Burrows-Wheeler Aligner (v.0.6.2), removed duplicate reads (PicardMarkDuplicates v.1.70), and performed indel realignment (GATK IndelRealigner v.1.6) and base-quality recalibration (GATK TableRecalibration v.1.6). We called variants using the GATK UnifiedGenotyper and flagged with VariantFiltration to mark potential false positives that did not pass the following filters: Heterozygous Allele Balance (ABHet) $>$ 0.75, Quality by Depth $>$ 5.0, Quality (QUAL) _ 50.0, Homopolymer Run (Hrun) $<$ 4.0, and low depth ($<$ 6x). We used SeattleSeq for variant annotation and the Combined Annotation Dependent Depletion (CADD) score to determine deleteriousness of identified missense variants.[49] Based on CADD score data for causal variants in other JS-associated genes, we used a CADD score cutoff of 15 to define deleterious variants.[47]

LR09-023 was ascertained as part of a larger study of genetic causes for Dandy-Walker malformation (DWM). Exome sequencing of this individual and his parents was performed by Beckman Coulter genomics as follows: genomic DNA isolated from peripheral blood was captured using the Agilent SureSelect V5 enrichment kit and sequenced on an Illumina HiSeq 2000 as 150-bp paired-end runs. Reads were aligned with BWA; variants were called with GATK and freebayes. Variants called by both GATK and freebayes were annotated using Gemini,[50] including datasets from the ExAC Exome,[51] NHLBI 6500 Exome,[52] and 1000 Genomes projects for variant frequencies, and amino-acid-change functional predictions from CADD scores.[49] Variants were filtered for de novo, recessive (compound heterozygous or homozygous), or X-linked inheritance, $<$0.001 frequency in public databases, predicted to be deleterious by CADD $>$ 10, and expressed in human fetal (BrainSpan[53]) or adult (GTex[54]) cerebellum.

For the two families in the Saudi Arabian cohort, DNA from the affected individuals as well as their unaffected siblings and parents were genotyped using the Axiom SNP Chip platform to determine the candidate autozygome.[55,56] The previously described "Mendeliome" targeted sequencing assay was then performed on DNA from affected members to search for likely causal variants in the known JS genes followed by whole-exome sequencing in samples without causal variants.[57] WES was performed using TruSeq Exome Enrichment kit (Illumina) following the manufacturer's protocol. Samples were prepared as an Illumina sequencing library, and in the second step, the sequencing libraries were enriched for the desired target using the Illumina Exome Enrichment protocol. The captured libraries were sequenced using an Illumina HiSeq 2000 Sequencer. The reads were mapped against UCSC hg19 by BWA. SNPs and indels were detected by SAMTOOLS. Homozygous rare, predicted-deleterious, and coding/splicing variants within the autozygome of the affected individual were considered as likely causal. We defined rare variants as those with frequency of $<$0.1% in publicly available variant databases (1000 Genomes, Exome Variant Server, and gnomAD) as well as a database of 2,379 in-house ethnically matched exomes, and defined deleterious if predicted to be pathogenic by PolyPhen, SIFT, and CADD (score $>$ 15).

Array CGH

To assess copy-number variation, we performed array comparative genomic hybridization using a custom 8x60K oligonucleotide array (Agilent Technologies)[58] targeting *AHI1*, *ARL13B*, *ARMC9*, *B9D1*, *B9D2*, *C2CD3*, *C5ORF42*, *CBY1* (MIM: 607757), *CC2D2A*, *CEP104* (MIM: 616690), *CEP120* (MIM: 613446), *CEP290*, *CEP41* (MIM: 610523), *CEP83* (MIM:615847), *CSPP1*, *DDX59* (MIM: 615464), *EXOC8* (MIM: 615283), *HYLS1* (MIM:610693), *IFT172*, *INPP5E*, *KCTD10* (MIM: 613421), *KIAA0556* (MIM: 616650), *KIAA0586* (MIM: 610178), *KIAA0753* (MIM: 617112), *KIF7*, *MKS1*, *NPHP1*, *NPHP3* (MIM: 608002), *NPHP4* (MIM: 607215), *OFD1*, *PDE6D*, *PIBF1* (MIM: 607532), *POC1B* (MIM: 614784), *RPGRIP1L*, *TBC1D32* (MIM: 615867), *TCTN1*, *TCTN2*, *TCTN3*, *TMEM107* (MIM: 616183), *TMEM138*, *TMEM17* (MIM: 614950), *TMEM216*, *TMEM218*, *TMEM231*, *TMEM237*, *TMEM67*, *TTC21B*, and *ZNF423*. Probe spacing was a median of 11 bp in the exons, and a median of 315 bp throughout the intronic regions and 100 kb on either side of each gene. Data were generated on an Agilent Technologies DNA Microarray Scanner with Surescan High-Resolution Technology using Agilent Scan Control software and were processed and analyzed using Agilent Feature Extraction and Agilent Cytogenomics software.

RNA Isolation and Quantitative PCR

We cultured human fibroblasts from healthy controls in DMEM + 10% fetal bovine serum (FBS) and 1% penicillin/streptomycin under standard conditions.[59–61] To induce ciliogenesis, we cultured in DMEM without FBS once the cells reached ~70% confluency. After treatment with 0.05% trypsin, cycling cells and serum-starved cells were harvested and RNA extracted using the Aurum Total RNA Mini Kit (Bio-rad). We generated cDNA from 2 μg of total RNA using the iScript Reverse Transcription Supermix for RT-qPCR (Biorad). The expression of *ARL13B* and *ARMC9* mRNAs was determined using qPCR. Each cDNA sample was amplified using Power SYBR Green PCR Master Mix (Applied Biosystems, Thermo Fisher Scientific) on the C1000 Thermal Cycler CFX (Bio-rad). After an initial denaturation of 10 min at 95°C, each cycle (x39) consisted of denaturation at 95°C for 15 s and anneal/extend at 60°C for 1 min with a plate read. The primers for *ARL13B* and *ARMC9* are listed in Table S1. *GAPDH* was used as an endogenous control to normalize each sample. The experiment was performed in triplicate.

Cell Lines, Antibodies, and Microscopy

Human telomerase-immortalized retinal pigment epithelium (hTERT-RPE1) cells were grown in DMEM (PAA) supplemented with F12 in a 1:1 ratio with 10% fetal bovine serum and 1% penicillin/streptomycin. Cells were plated on glass coverslips for immunofluorescence imaging. At 24 hr after plating, cells were serum starved for 48 hr in 0.2% FBS medium to induce cell cycle arrest and ciliogenesis. Cells were rinsed once with 1× PBS at room temperature and then fixed in 2% paraformaldehyde for 20 min and permeabilized with 1% Triton-X for 5 min. Cells were blocked in freshly prepared 2% bovine serum albumin for 45 min and then incubated with the following antibodies for 1 hr: rabbit anti-ARMC9 (Atlas Antibodies cat# HPA019041, RRID: AB_1233489; 1:200), guinea pig anti-RPGRIP1L (SNC040, 1:300), a monoclonal anti-acetylated tubulin (clone 6-11-B1, Sigma-Aldrich, T6793; 1:1,000), and a mouse monoclonal anti-γ-tubulin (Sigma T5326, 1:500). Anti-ARMC9 recognizes an epitope at the N-terminal portion of the protein. Cells were stained with secondary antibodies for 45 min. The following secondary antibodies were used (all from Life Technologies/Thermo Fisher Scientific; all diluted 1:500 in 2% BSA): anti-guinea pig IgG Alexa Fluor 647, anti-rabbit IgG Alexa Fluor 488, and anti-mouse IgG Alexa Fluor 568. DAPI (4′,6-diamidino-2-phenylindole) stained the nucleus. Confocal imaging was done with the Zeiss LSM 880 Laser scanning microscope equipped with Airyscan technology.

Antibody Validation with siRNA Knock Down

Reverse transfections on hTERT-RPE1 cells were performed with pre-designed Silencer Select siRNA to *ARMC9* (Ambion from Life Technologies), as well as a positive control to knock down *GAPDH* (Ambion from Life Technologies) and a scrambled non-targeting negative control (Ambion from Life Technologies). Lyophilized siRNAs were re-constituted with RNase-free water (Thermo Scientific) to a final working concentration of 50 nM. Lipofectamine RNAiMax (LifeTechnologies) and Opti-MEM (LifeTechnologies) were used for siRNA transfection and done in accordance with the manufacturer's protocol. Cells were harvested and lysed with RIPA lysis buffer supplemented with Complete Protease Inhibitor Cocktail Tablets (Roche) 72 hr after transfection and western blotting was performed. Primary antibodies mouse monoclonal GAPDH (Thermo Scientific) and rabbit polyclonal ARMC9 (Human Protein Atlas Sigma Aldrich) were used at 1:1,000 and 1:500 dilutions, respectively, and incubated overnight at 4°C. Secondary antibodies goat anti-rabbit IRDye800 (LI-COR Biosciences) and goat anti-mouse IRDye680 (LI-COR Biosciences) were used at a dilution of 1:10,000 and incubated with blots for 1 hr at room temperature. Imaging was done with the Odyssey CLx imaging system (LI-COR Biosciences). Protein quantification was performed using Image Studio Lite software (LI-COR Biosciences).

Zebrafish In Situs, CRISPR, Mutation Assay, and Histology

Zebrafish were maintained at 28°C with a 14 hr/10 hr light/dark cycle as previously described.[62] All zebrafish protocols were in compliance with internationally recognized guidelines for the use of zebrafish in biomedical research, and the experiments were approved by local authorities (Veterinäramt Zürich TV4206).

In situ hybridization was performed following standard protocols with a probe spanning over 800 bp at the 3′ end of *armc9* generated using the primers 5′-AGCTCAACTCAGCGACCATC-3′ and 3′-TGCTGTTACAGGAAGCTGGA-5′. sgRNAs for CRISPR/Cas9 mutagenesis were designed using the CHOPCHOP website: 3′-GGGATTGGGCACAAATGGCA-5′ and 3′-GGAACAGCTCCTGAAAGGAC-5′ for exon 4 and 5′-GGTCAAAGAGCTGAATGACT-3′ and 3′-GGAGCTCCGTCAGGACTTTC-5′ for exon 14/15. Pairs of sgRNAs for each target site were mixed with Cas9 protein (gift from Darren Gilmour) and injected into 1-cell stage embryos obtained through natural matings. Individual larvae were lysed for assessment of mutagenesis efficiency. Amplification of the target regions for genotyping was performed using primer pairs 5′-CAGCCAAACCACTGAGTTCC-3′ and 3′-TGACCCTGTAGTGTGTGCGTA-5′ for exon 4 and 5′-CACGCCTTGCACCACACT-3′ and 3′-CACTCCCCTGTTTGAGCAAT-5′ for exons 14/15. The PCR products were analyzed on gel electrophoresis and bands were cut out and subcloned before sequencing. The remaining F0 fish were raised. Brains of four F0 fish with curved bodies were dissected out at 5 months of age, halved, and fixed in 2.5% Glutaraldehyde in 0.1 M Cacodylate buffer and prepared for scanning electron microscopy (SEM) following standard protocols. SEM was performed on a ZEISS Supra VP 50 microscope. Cryosections were performed according to standard protocols and IHC was performed as previously described,[37,62] using the zpr1 antibody.[63] Vybrant DiO (ThermoFisherScientific) and DAPI were used for counterstaining. Images were acquired on a Leica HCS LSI confocal microscope. Histological sections using Technovit were performed as previously described.[62] Images were acquired on an Olympus BX61 microscope.

Results

Exome Sequencing Reveals *ARMC9* Mutations as a Cause for JS

To identify novel genetic causes of JS, we performed whole-exome sequencing on a cohort of 53 individuals (51 families) with a clinical diagnosis of JS enrolled in the University of Washington (UW) Joubert Syndrome Research Program. Inclusion criteria comprised the presence of clinical findings of JS (developmental delays, hypotonia, ataxia, and/or oculomotor apraxia), diagnostic brain imaging findings, and lack of mutations in 28 JS-associated genes (*NPHP1*, *AHI1*, *CEP290*, *RPGRIP1L*, *TMEM67*, *CC2D2A*, *ARL13B*, *INPP5E*, *OFD1*, *TMEM216*, *CEP41*, *TMEM237*, *TCTN2*, *KIF7*, *TCTN1*, *TMEM138*, *MKS1*, *C5ORF42*, *TMEM231*, *TCTN3*, *CSPP1*, *PDE6D*,

Table 1. Phenotypic Features of Individuals with *ARMC9*-Related Joubert Syndrome with Mutations

ID#	UW132-3	UW132-4	UW348-3	UW116-3	UW335-3	UW335-4	UW349-3	LR09-023	SA1-3	SA2-3	SA2-4
Gene	*ARMC9*	*ARMC9*	*ARMC9*	*ARMC9*	*ARMC9*	*ARMC9*	*ARMC9*	*ARMC9*	*ARMC9*	*ARMC9*	*ARMC9*
Mutation 1	c.205G>A (p.Gly69Arg)	c.205G>A (p.Gly69Arg)	c.51+5G>T (splice)	c.1027C>T (p.Arg343Cys)	c.259C>T (p.Arg87*)	c.259C>T (p.Arg87*)	c.1474+1G>C (splice)	c.1474G>A (p.Gly492Arg)	c.1027C>T (p.Arg343Cys)	c.1559C>T (p.Pro520Leu)	c.1559C>T (p.Pro520Leu)
MAF	0.000025 (7/277212)	0.000025 (7/277212)	ND	ND	0.000018 (5/277214)	0.000018 (5/277214)	ND	ND	0.000053 (13/246244)	0.0000041 (1/246192)	0.0000041 (1/246192)
CADD v1.3	33	33	14.54	N/A	35	35	23.5	26	34	34	34
Parent	paternal	paternal	unable	maternal	paternal	paternal	maternal	maternal	maternal	maternal	maternal
Mutation 2	c.1336C>T (p.Arg446Cys)	c.1336C>T (p.Arg446Cys)	c.51+5G>T (splice)	c.1211_1334del (p.Arg405Alafs*7)	c.1027C>A (p.Arg343Ser)	c.1027C>A (p.Arg343Ser)	c.1027C>T (p.Arg343Cys)	c.1027C>T (p.Arg343Cys)	c.1027C>T (p.Arg343Cys)	c.1559C>T (p.Pro520Leu)	c.1559C>T (p.Pro520Leu)
AF	0.0000041 (1/246076)	0.0000041 (1/246076)	ND	0.000053 (13/246244)	0.0000041 (1/246244)	0.0000041 (1/246244)	0.000053 (13/246244)	0.000053 (13/246244)	0.000053 (13/246244)	0.0000041 (1/246192)	0.0000041 (1/246192)
CADD v1.3	34	34	14.54	34	34	34	34	34	34	34	34
Parent	maternal	maternal	unable	paternal	maternal	maternal	paternal	paternal	paternal	paternal	paternal
Ethnicity/ country	white/US	white/US	white/Israel	white/US	white/ Australia	white/ Australia	>1 race/US	white/US	Arab/Saudi	Arab/Saudi	Arab/Saudi
Gender	F	M	F	F	F	M	M	M	M	F	M
Age (years)	33	29	10	8	5	7	2	8	7	4	5
Dev. disability	y	y	y	y	y	y	y	y	y	y	y
Apnea/tachyp	n	n	unk	both	both	n	A	T	y*	n	y*
Abnl eye mvts	y	y	y	y	y	y	y	unk	y	y	n
Retinal dystrophy	n	n	y	n	n	n	n	unk	unk	y	n
Kidney	n	n	unk	unk	n	n	n	unk	n	n	n
Liver	n	n	unk	unk	n	n	n	unk	n	n	n
Polydactyly	n	y	unk	n	n	n	n	n	n	y	n
Coloboma	n	n	unk	n	n	n	n	unk	unk	n	n
Ptosis	n	y	unk	y	n	n	y	y	y	y	y

(*Continued on next page*)

Table 1. *Continued*

ID#	UW132-3	UW132-4	UW348-3	UW116-3	UW335-3	UW335-4	UW349-3	LR09-023	SA1-3	SA2-3	SA2-4
Seizures	y	n	n	y	n	n	n	n	n	n	n
Other	hysterectomy 2016 (heavy bleeding); worsening visual acuity; seizures	lithium-induced hypo-thyroidism; L foot postaxial polydactyly	abnormal ERG	G-tube	–	single heterotopia (left occipital horn)	micrognathia; high palate; bifid uvula; bilateral optic nerve hypoplasia; GH deficiency; micropenis; eyelid implants; possible hearing loss; borderline HSM	Dandy Walker malformation; ventriculo- and cysto-peritoneal shunts; non-ambulatory; non-verbal at age 8 years	–	broad nasal bridge; thin upper lip; Y-shaped 2/3 toe syndactyly	–

Abbreviations are as follows: A, apnea; AF, allele frequency based on gnomAD;[51] ERG, electroretinogram; F, female; GH, growth hormone; HSM, hepatosplenomegaly; ID, identification; M, male; n, no; ND, not documented; T, tachypnea; unk, unknown; y, yes. Asterisk (*) indicates transient neonatal.

IFT172, *ZNF423*, *TTC21B*, *B9D1*, *B9D2*, and *C2CD3*) based on targeted sequencing.[46,47] Variants from the exome-sequencing data that were rare (minor allele frequency < 1% in the exome variant server [EVS] database) and predicted to be deleterious (stop-gain, frameshift, canonical splice variants, and variants with CADD score > 15) were retained for further analysis.

We identified pairs of siblings in two families that shared two rare, predicted-deleterious variants (RDVs) in *ARMC9* (GenBank: NM_025139.4): UW132-3 and -4 carry c.205G>A (p.Gly69Arg) and c.1336C>T (Arg446Cys) and UW335-3 and -4 carry c.259C>T (p.Arg87*) and c.1027C>A (p.Arg343Ser) (Table 1 and Figure 1).

We then performed targeted sequencing of *ARMC9* using the Molecular Inversion Probe (MIPs) capture method followed by next generation sequencing on samples from 534 individuals in 456 families with and without known causes. Three additional individuals in three families have *ARMC9* RDVs: UW348-3 has a homozygous c.51+5G>T, predicted splice variant, UW349-3 has two RDVs (predicted splice c.1474+1G>C and missense c.1027C>T [p.Arg343Cys]), and UW116-3 has a single heterozygous c.1027C>T (p.Arg343Cys). Based on decreased sequence coverage for two consecutive MIPs covering exon 14 in UW116-3, we suspected a deletion in UW116-3. We performed comparative genomic hybridization using a custom array targeting the JS genes[58,64,65] and identified a 2.5 kb deletion encompassing exon 14 in UW116-3 (Figures 1B–1D). Exon 14 is 124 bp long, so its loss is predicted to result in a frameshift and truncation of the protein or nonsense-mediated decay of the transcript.

In parallel, exome sequencing in two other cohorts identified biallelic RDVs in *ARMC9*: three individuals (SA1-3, SA2-3, and SA2-4) from two families in a cohort of 47 Saudi Arabian families[66] affected by JS had homozygous *ARMC9* missense RDVs (c.1027C>T [p.Arg343Cys] and c.1559C>T [p.Pro520Leu]) and a single individual with JS (LR09-023) from a mixed cohort of 100 individuals with Dandy-Walker malformation and cerebellar hypoplasia had compound heterozygous *ARMC9* RDVs (c.1474G>A [p.Gly492Arg] and c.1027C>T [p.Arg343Cys]). In total, we identified 10 different *ARMC9* RDVs (1 stop-gain, 2 splice, 6 missense, and 1 single exon deletion) in 11 individuals from 8 families. All variants were validated by Sanger sequencing, and for ten individuals from seven families their segregation with the disease was confirmed in parents and siblings; segregation was not performed in the remaining family because DNA was not available from parents (Table 1). c.1027C>T (p.Arg343Cys) appears to be a recurrent mutation rather than a founder variant, since it is present in families of diverse ethnicities, and a second variant (c.1027C>A [p.Arg343Ser]) affects the same position. ARMC9 is predicted to have a Lissencephaly type-1-like homology (LisH) motif, a coiled-coil domain, and armadillo repeats (Figure 1A). Two of the missense RDVs

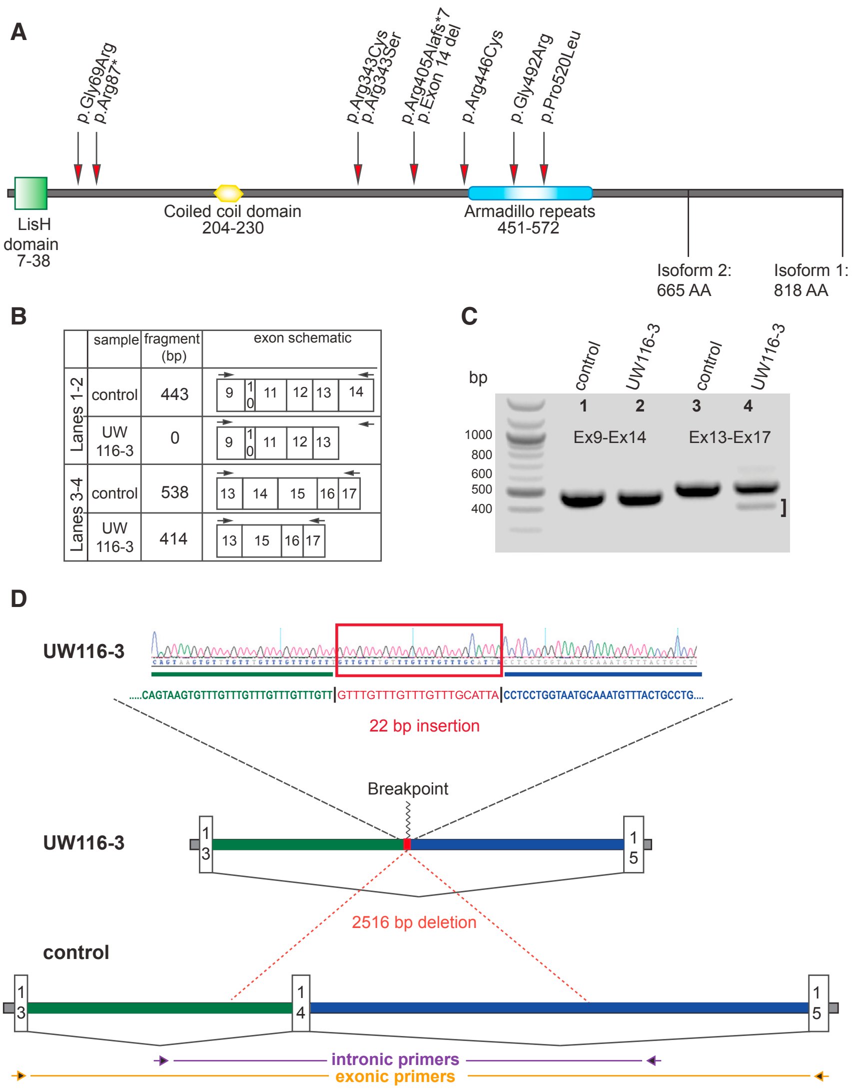

Figure 1. ***ARMC9*** **Mutations Cause JS**

(A) The *ARMC9* gene encodes a protein with an N-terminal LisH domain (green square), a coiled coil domain (yellow polygon), and a series of armadillo repeats (blue oval). Patient mutations are indicated by red arrows.

(B–D) Confirmation of *ARMC9* exon 14 deletion in UW116-3. No difference in the size or number of PCR products is observed between cDNA isolated from UW116-3 and two unaffected control cell lines using primers in exons 9 and 14 (C and D). Primers in exons 13 and 17 amplify a full-length product and a shorter product (bracket) in UW116-3, but only the full-length product in the two control lines. Sequencing genomic DNA amplified by primers flanking exon 14 reveals a 2,516 bp deletion with a 22 bp insertion (D).

are in the armadillo repeats, and the other four missense RDVs are not located in known domains.

ARMC9-Related JS Is Indistinguishable from JS due to Other Genetic Causes

All of the affected individuals have typical features of JS including hypotonia and developmental disability, most severely affecting motor and speech function (Table 1). Ages range from 2 to 33 years. Most of the individuals have isolated neurodevelopmental issues, including two with seizures (UW132-3 and UW116-3). Two individuals (UW132-4 and SA2-3) have postaxial polydactyly, and SA2-3 also has syndactyly. Two individuals (UW348-3 and SA2-3) also have retinal dystrophy, but none have kidney or liver involvement. UW349-3 has a more complex presentation with hypopituitarism, bilateral optic nerve hypoplasia, bifid uvula, and an abnormal brainstem (see below).

Based on direct review of the brain MRIs, all of the affected individuals have the "molar tooth sign" as well as dysplasia of the superior cerebellar folia (Figures 2A, 2B, 2F, and Table S2). Three individuals (UW335-4, LR09-023, and SA2-3) have cerebellar hemisphere dysplasia, seen in up to 1/3 of individuals with JS (Figure 2C).[67] In addition to the MTS, LR09-023 has a large posterior fossa with a rotated cerebellar vermis consistent with Dandy-Walker malformation (Figures 2D, 2E, and 2I). LR09-023 also has a single periventricular heterotopia (Figure 2D), as do UW116-3 and UW335-4. The two oldest individuals (UW132-3 and -4) have an atrophic appearance to their cerebellum, more severely affecting the vermis than the hemispheres (Figure 2G). UW349-3 has a kinked brainstem and cervicomedullary junction heterotopia (Figure 2H) seen in a small subset of individuals with JS,[67–71] and UW349-3 and SA2-3 have an absent posterior pituitary bright spot, but only UW349-3 has known pituitary insufficiency.

ARMC9 Localizes to the Basal Bodies of Primary Cilia

JS-associated proteins have been shown to localize in and around primary cilia;[40,45,72–74] therefore, we used a commercially available ARMC9 antibody to evaluate endogenous ARMC9 localization in ciliated hTERT-RPE1 cells. ARMC9 localized to the ciliary basal body (Figure 3A, white arrowhead), basal to but not overlapping with the transition zone marker RPGRIP1L, as well as to the daughter centriole (Figure 3A, white arrow) marked by acetylated α-tubulin antibody (Figure 3A). ARMC9 co-localizes with γ-tubulin at the basal body (Figure 3B, white arrow), proximal to RPGRIP1L, and at the daughter centriole (Figure 3B, white arrowhead).

ARMC9 Expression Is Upregulated in Ciliated Cells

Based on data from model systems and humans, many genes involved in cilium function are upregulated in

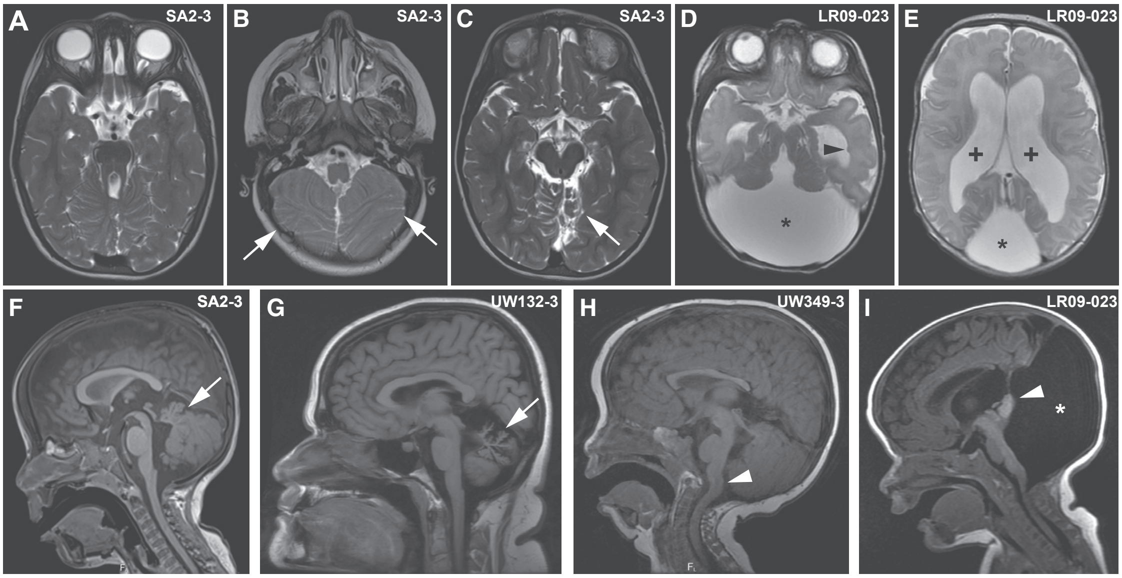

Figure 2. Brain Imaging Findings in Individuals with *ARMC9*-Related Joubert Syndrome
(A–C) MTS (A), inferior cerebellar dysplasia (white arrows in B), and superior cerebellar dysplasia (white arrow in C) in SA2-3.
(D and E) MTS (D), posterior fossa cyst (asterisks in D and E), and ventriculomegaly (plus signs in E) in LR09-023. Note the single periventricular nodular heterotopia (black arrowhead in D).
(F) Vermis hypoplasia and elevated roof of the 4th ventricle in SA2-3 (white arrow).
(G) Cerebellar vermis hypoplasia and atrophy in UW132-3 (white arrow).
(H) Kinked brainstem and cervicomedullary heterotopia in UW349-3 (white arrowhead).
(I) Enlarged posterior fossa fluid collection (white asterisk) and rotated vermis (white arrowhead) in LR09-032.
Axial T2-weighted images in (A)–(E); sagittal T1-weighted images in (F)–(I).

ciliated cells.[75–79] We evaluated *ARMC9* expression by quantitative PCR in control human fibroblasts with and without serum in the medium. In the presence of serum, fibroblasts actively divide and few have cilia, but in response to serum starvation, 80%–90% drop out of the cell cycle and make cilia, similar to other published results.[80] *ARMC9* expression was 2.0- to 2.7-fold higher in serum-starved cells than in cells grown with serum (Figure 3C). For comparison, expression of another JS-associated gene, *ARL13B*, was 2.4-fold higher in serum-starved cells.

Zebrafish *armc9* Mutants Display Typical Ciliopathy Phenotypes

To investigate the function of ARMC9 in vivo, we turned to the zebrafish model. Zebrafish have a single *ARMC9* ortholog that has 58% identity and 72% similarity with the human protein. Based on database predictions and manual curation, both the LisH domain and the armadillo-fold domain are conserved in zebrafish at similar positions to the human protein (amino acids 7–39 and 375–600, respectively) (Figure S1). In adult zebrafish, *armc9* is expressed in multiple CNS regions based on in situ hybridization, including the cerebellum (Figure S1), all periventricular regions (Figure 4A), and all layers of the retina (Figure 4B). To explore whether loss of *armc9* function results in ciliopathy phenotypes, we engineered frameshift mutations in zebrafish using CRISPR/Cas9 (Figure S2). Co-injecting pairs of small guide RNAs targeting either exon 4 or exons 14–15 (the latter corresponding to the middle of the armadillo-fold domain), we generated mutations with very high efficiency (91% of sequenced clones from individual F0 larvae carried indels, the majority of which were out-of-frame; Figure S2). Of approximately 140 surviving F0 fish raised, 10 developed a curved body axis around 6 weeks of age (Figures 4C and 4D), including both exon 4- and exon 14-15-targeted animals. The body curvature phenotype correlated well with the presence of indels affecting the targeted exons; genotyping of 49 F0 fish by gel electrophoresis demonstrated various *armc9* indels in 11 fish, only 1 of which did not have a curved body shape. Moreover, such body curvature was never observed in hundreds of raised F0 fish injected with sgRNA targeting non-ciliary genes (20 different sgRNAs). A recent study suggested body curvature in zebrafish is caused by deficient ependymal cilia-generated cerebrospinal fluid (CSF) flow.[81] Indeed, using SEM we observed a substantial reduction of cilia numbers on the ventricular surface of adult zebrafish harboring *armc9* mutations (Figures 4E and 4F). In addition, a subset of F0 fish with body curvature also displayed a retinal coloboma and had shortened photoreceptor outer segments, typical phenotypes observed with ciliary dysfunction (Figures 4G–4J and S2).[38] Taken together, these results confirm that *armc9* loss of function in zebrafish causes typical ciliopathy phenotypes and strongly support a role for *armc9* in ciliary function.

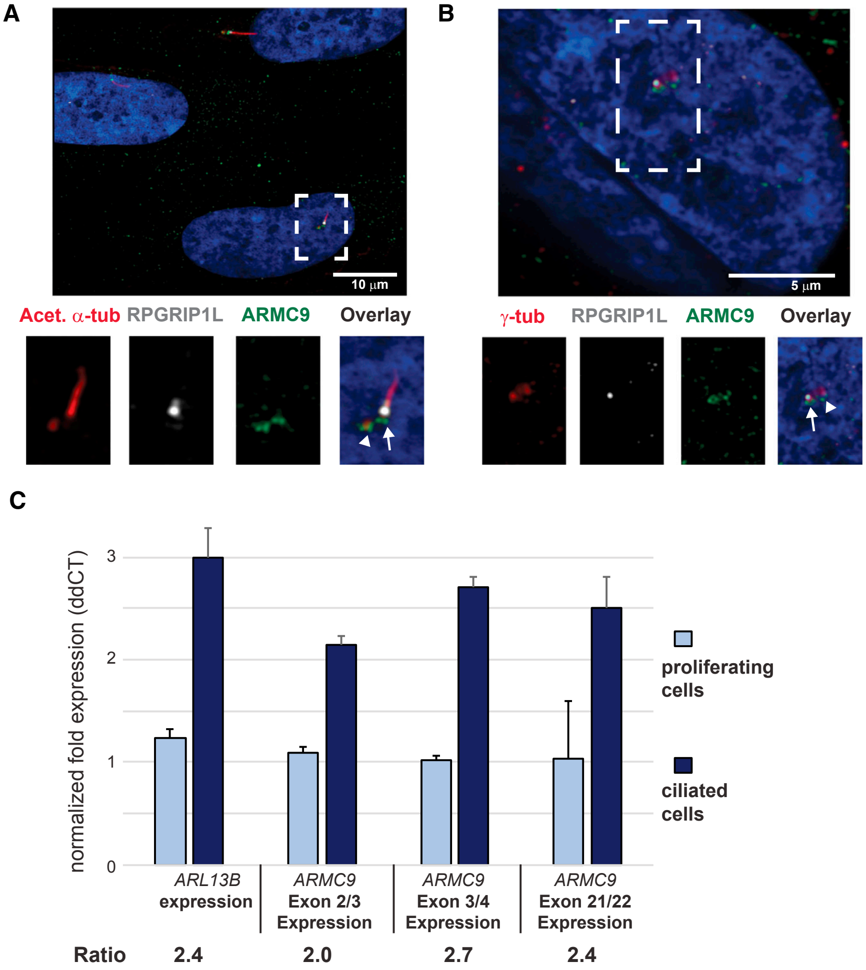

Figure 3. ARMC9 Localization and *ARMC9* Expression in Ciliated and Proliferating Cells

(A) ARMC9 (green) localizes at the basal body (white arrow) and at the daughter centriole (white arrowhead) of the primary cilium in serum-starved hTERT RPE1 cells. The ciliary marker anti-RPGRIP1L (white) marks the ciliary transition zone and anti-acetylated α-tubulin (red) marks the ciliary axoneme.

(B) ARMC9 (green) co-localizes with γ-tubulin (red) at the ciliary basal body in serum-starved hTERT RPE1 cells. Anti-RPGRIP1L marks distal to the basal body (white) and DAPI (blue) stains the nuclei.

(C) *ARMC9* expression in control human fibroblasts grown with serum (proliferating cells) and without serum (ciliated cells), assessed using qPCR with *GAPDH* as a reference gene. *ARL13B* is used as a positive control for a gene upregulated in ciliated cells.

Error bars indicate standard deviation.

Discussion

Mutations in more than 35 genes have been identified in individuals with JS, explaining the genetic cause in 62% to 97% of case subjects, depending on the study.[47,66,82] In addition to these known causes, we now identify *ARMC9* mutations as an additional cause of JS accounting for almost 1% of families in our cohort of >500. Substantial functional evidence supports *ARMC9* as a ciliopathy-associated gene.

ARMC9 Localizes to the Basal Body

We provide evidence that ARMC9 localizes to the ciliary basal body, similar to other JS-associated proteins (Figures 3A and 3B). The basal body originates from the mother centriole that docks at the cell membrane during interphase to nucleate the ciliary axoneme. The daughter centriole remains tethered to the basal body by an interconnecting fiber, and both structures often appear as juxtaposed puncta on immunofluorescence images. Basal bodies are composed of nine short triplet microtubules arranged in a circle, and two of the three microtubules in each basal body triplet extend as axonemal microtubules. Several other JS-associated proteins (OFD1, KIAA0586, and C2CD3) also localize to the basal body.[40,45,72–74,83] Strikingly, ARMC9 and OFD1 both have an N-terminal LisH motif that is known to bind to microtubules (Figure 1A).[72,84,85] Two published proteomic studies in murine inner medullary collecting duct (IMCD3) cells also provide support for ARMC9 as a cilium-associated protein: (1) ARMC9 was detected a total of 31 times across ciliary fractions via MudPIT mass spectrometry of isolated cilia[86] and (2) proximity labeling using a promiscuous biotinylating enzyme conjugated to the transition zone protein NPHP3 detected ARMC9-specific peptides (6 spectral counts), thus providing direct evidence for their adjacency.[87]

ARMC9 Is Present in Ciliated Organisms and Upregulated in Ciliated Cells

The use of comparative genomics to compile genes exclusively present in ciliated organisms versus non-ciliated organisms is a common technique in identifying ciliary genes.[88,89] *ARMC9* homologs are present in ciliated eukaryotes from humans to unicellular flagellates such as *Trochaic trifallax* but absent in plants, fungi, bacteria, viruses, and Archaea.[90] Expression of the *ARMC9 C. elegans* homolog, F59G1.4, is restricted to sensory neurons, the only ciliated cells in this organism.[91–93] Ciliary gene induction was first linked to ciliogenesis in classical experiments in unicellular flagellates, notably *Chlamydomonas*, a model system particularly well suited to study ciliary biology. These experiments demonstrated that new protein synthesis was required for full cilia regeneration via use of protein synthesis inhibitors or enucleating cells.[75,76] Later experiments show that ciliary genes are widely induced during

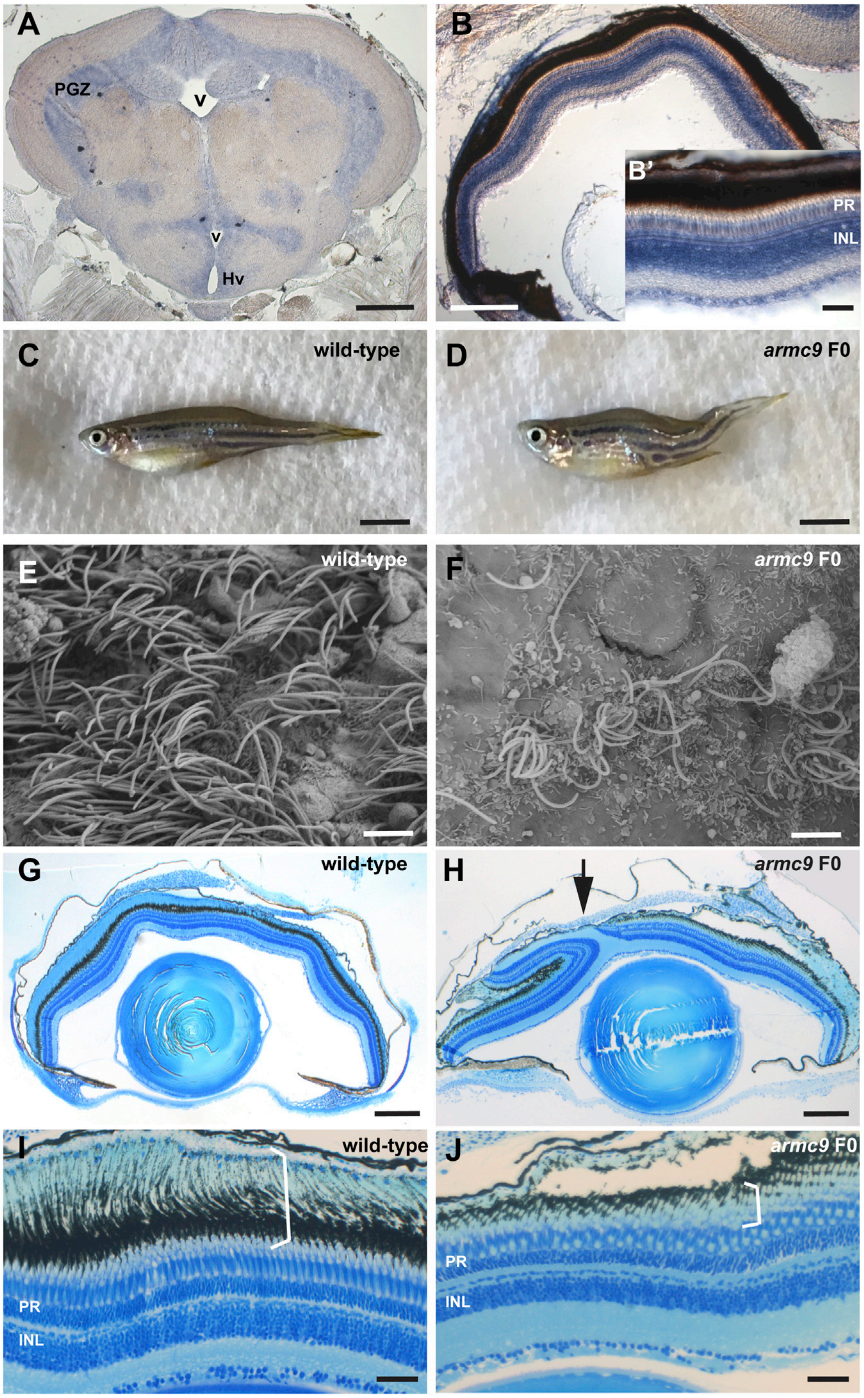

Figure 4. *armc9* Loss of Function in Zebrafish Leads to Typical Ciliopathy Phenotypes

(A and B) Expression of *armc9* in zebrafish adult brain (A) and retina (B) by in situ hybridization. Note the expression along ventricular surfaces in (A) and in all retinal layers, including the photoreceptor (PR) and the inner nuclear layer (INL) (B, B′).

(C and D) Adult zebrafish harboring *armc9* mutations display a curved body shape (D) compared to wild-type controls (C).

(E and F) Scanning electron microscopy image of the ventricular surface demonstrates bundles of cilia in wild-type (E) but substantial reduction of cilia numbers in F0 *armc9* fish (F).

(G and H) Histological sections through adult zebrafish eyes of wild-type (G) and F0 *armc9* mutants (H) showing a coloboma (arrow).

(I and J) Higher-magnification images show the different retinal layers in wild-type fish (I) including the PRs and their long outer segments (OS, bracket) which represent highly specialized ciliary compartments. (J) Note the shortened OS in F0 *armc9* mutants (bracket).

Scale bars are 200 μm in (A) and (B), 50 μm in (B′), 5 mm in (C) and (D), 3 μm in (E) and (F), 250 μm in (G) and (H), and 50 μm in (I) and (J). Abbreviations are as follows: v, ventricle; PGZ, periventricular gray zone of optic tectum; Hv, ventral zone of periventricular hypothalamus; PR, photoreceptors; INL, inner nuclear layer.

ciliogenesis and maintained at high levels in ciliated cells.[77–79] Ciliary genes are similarly upregulated in higher organisms.[36,94,95] Similar to other ciliary genes, we demonstrate that *ARMC9* expression is upregulated in human ciliated fibroblasts, as compared to cycling cells (Figure 3C).

Zebrafish Harboring *armc9* Mutations Display Typical Ciliopathy Phenotypes

In a vertebrate model, zebrafish harboring CRISPR-engineered *armc9* mutations display phenotypes similar to those seen with loss of function for zebrafish orthologs of other ciliopathy-associated genes (Figure 4).[38,96,97] The retinal dystrophy and/or curved body axis are also seen in loss-of-function models for the *cc2d2a*, *ahi1*, and *ift* genes.[38,97–100] Furthermore, we show a strong reduction of cilia in the brain ventricles of zebrafish harboring *armc9* mutations, suggesting that the gene product may participate in early stages of ciliogenesis or be required for ciliary maintenance. The mosaic state of the animals analyzed in this work does not allow for discrimination between these two possibilities. Indeed, the presence of residual cilia on some ventricular cells may be explained by lack of *armc9* mutations in those cells or by incomplete penetrance of the phenotype. Future analysis of stable lines will help address these possibilities. The identical phenotypes observed in multiple animals generated using guides targeting different *armc9* regions, combined with the lack of these phenotypes with CRISPR/Cas9-generated deletions in 20 different non-ciliary genes, strongly supports the specificity of the observed phenotypes and argues against non-specific or off-target effects of CRISPR/Cas9.

In conclusion, we demonstrate that mutations in *ARMC9* cause JS and show that ARMC9 localizes to the basal body. Given the LisH domain, ARMC9 likely binds microtubules there, but the details of its function remain to be elucidated. Delineating all of the genes involved in JS will enable future work to determine how proteins that localize to the basal body, transition zone, cilium proper, and cilium tip all contribute to the molecular mechanism(s) underlying JS. Understanding the molecular mechanisms of JS will lead to more specific treatments in the future and further our understanding of basic ciliary biology in health and disease.

Accession Numbers

The disease-associated variants described in this paper have been uploaded to ClinVar under accession numbers SCV000579394–SCV000579403, available after June 26, 2017.

Supplemental Data

Supplemental Data include three figures and two tables and can be found with this article online at http://dx.doi.org/10.1016/j.ajhg.2017.05.010.

Acknowledgments

We deeply thank the families who participated in this study. We also thank the Joubert syndrome and Related Disorder Foundation for referring families, Heather Mefford and her laboratory for help with arrays, the Center for Microscopy and Image Analysis, University of Zurich (ZMB), for their assistance with Scanning Electron Microscopy, in particular Gery Barmettler, the Genotyping and Sequencing Core Facilities at King Faisal Specialist Hospital & Research Centre for their technical help, and Darren Gilmour for the Cas9 protein. This work was supported by the following: NIH Eunice Kennedy Shriver National Institute of Child Health and Human Development U54HD083091 (Genetics Core and Sub-project 6849) to D.D., NIH National Institute of Neurological Diseases and Stroke (R01NS064077 to D.D. and R01NS050375 to W.B.D.), private donations from families to D.D., the Swiss National Science Foundation (PZ00P3_163979) to R.B.-G., the Netherlands Organization for Scientific Research (NWO Vici-865.12.005) to R.R., the King Salman Center for Disability Research to F.S.A., Dandy-Walker Alliance to W.B.D., and NIH National Human Genome Research Institute (U54HG006493) to M.B. and D.N. We acknowledge the support of the Saudi Human Genome Program (F.S.A.).

Received: April 10, 2017
Accepted: May 11, 2017
Published: June 15, 2017

Web Resources

Burrows-Wheeler Aligner, http://bio-bwa.sourceforge.net/
CADD, http://cadd.gs.washington.edu/
CHOPCHOP, http://chopchop.cbu.uib.no/
ClinVar, https://www.ncbi.nlm.nih.gov/clinvar/
NHLBI Exome Sequencing Project (ESP) Exome Variant Server, http://evs.gs.washington.edu/EVS/
OMIM, http://www.omim.org/
samtools, https://github.com/samtools/
SeattleSeq Annotation 137, http://snp.gs.washington.edu/SeattleSeqAnnotation137/
UCSC Genome Browser, http://genome.ucsc.edu

References

1. Valente, E.M., Logan, C.V., Mougou-Zerelli, S., Lee, J.H., Silhavy, J.L., Brancati, F., Iannicelli, M., Travaglini, L., Romani, S., Illi, B., et al. (2010). Mutations in TMEM216 perturb ciliogenesis and cause Joubert, Meckel and related syndromes. Nat. Genet. *42*, 619–625.
2. Tuz, K., Bachmann-Gagescu, R., O'Day, D.R., Hua, K., Isabella, C.R., Phelps, I.G., Stolarski, A.E., O'Roak, B.J., Dempsey, J.C., Lourenco, C., et al. (2014). Mutations in CSPP1 cause primary cilia abnormalities and Joubert syndrome with or without Jeune asphyxiating thoracic dystrophy. Am. J. Hum. Genet. *94*, 62–72.
3. Thomas, S., Legendre, M., Saunier, S., Bessières, B., Alby, C., Bonnière, M., Toutain, A., Loeuillet, L., Szymanska, K., Jossic, F., et al. (2012). TCTN3 mutations cause Mohr-Majewski syndrome. Am. J. Hum. Genet. *91*, 372–378.
4. Srour, M., Schwartzentruber, J., Hamdan, F.F., Ospina, L.H., Patry, L., Labuda, D., Massicotte, C., Dobrzeniecka, S., Capo-Chichi, J.M., Papillon-Cavanagh, S., et al.; FORGE Canada Consortium (2012). Mutations in C5ORF42 cause Joubert syndrome in the French Canadian population. Am. J. Hum. Genet. *90*, 693–700.
5. Srour, M., Hamdan, F.F., Schwartzentruber, J.A., Patry, L., Ospina, L.H., Shevell, M.I., Désilets, V., Dobrzeniecka, S., Mathonnet, G., Lemyre, E., et al.; FORGE Canada Consortium (2012). Mutations in TMEM231 cause Joubert syndrome in French Canadians. J. Med. Genet. *49*, 636–641.
6. Sayer, J.A., Otto, E.A., O'Toole, J.F., Nurnberg, G., Kennedy, M.A., Becker, C., Hennies, H.C., Helou, J., Attanasio, M., Fausett, B.V., et al. (2006). The centrosomal protein nephrocystin-6 is mutated in Joubert syndrome and activates transcription factor ATF4. Nat. Genet. *38*, 674–681.
7. Sang, L., Miller, J.J., Corbit, K.C., Giles, R.H., Brauer, M.J., Otto, E.A., Baye, L.M., Wen, X., Scales, S.J., Kwong, M., et al. (2011). Mapping the NPHP-JBTS-MKS protein network reveals ciliopathy disease genes and pathways. Cell *145*, 513–528.
8. Romani, M., Micalizzi, A., Kraoua, I., Dotti, M.T., Cavallin, M., Sztriha, L., Ruta, R., Mancini, F., Mazza, T., Castellana, S., et al. (2014). Mutations in B9D1 and MKS1 cause mild Joubert syndrome: expanding the genetic overlap with the lethal ciliopathy Meckel syndrome. Orphanet J. Rare Dis. *9*, 72.
9. Parisi, M.A., Bennett, C.L., Eckert, M.L., Dobyns, W.B., Gleeson, J.G., Shaw, D.W., McDonald, R., Eddy, A., Chance, P.F., and Glass, I.A. (2004). The NPHP1 gene deletion associated with juvenile nephronophthisis is present in a subset of individuals with Joubert syndrome. Am. J. Hum. Genet. *75*, 82–91.
10. Lee, J.H., Silhavy, J.L., Lee, J.E., Al-Gazali, L., Thomas, S., Davis, E.E., Bielas, S.L., Hill, K.J., Iannicelli, M., Brancati, F., et al. (2012). Evolutionarily assembled cis-regulatory module at a human ciliopathy locus. Science *335*, 966–969.

11. Lee, J.E., Silhavy, J.L., Zaki, M.S., Schroth, J., Bielas, S.L., Marsh, S.E., Olvera, J., Brancati, F., Iannicelli, M., Ikegami, K., et al. (2012). CEP41 is mutated in Joubert syndrome and is required for tubulin glutamylation at the cilium. Nat. Genet. *44*, 193–199.
12. Huang, L., Szymanska, K., Jensen, V.L., Janecke, A.R., Innes, A.M., Davis, E.E., Frosk, P., Li, C., Willer, J.R., Chodirker, B.N., et al. (2011). TMEM237 is mutated in individuals with a Joubert syndrome related disorder and expands the role of the TMEM family at the ciliary transition zone. Am. J. Hum. Genet. *89*, 713–730.
13. Halbritter, J., Bizet, A.A., Schmidts, M., Porath, J.D., Braun, D.A., Gee, H.Y., McInerney-Leo, A.M., Krug, P., Filhol, E., Davis, E.E., et al.; UK10K Consortium (2013). Defects in the IFT-B component IFT172 cause Jeune and Mainzer-Saldino syndromes in humans. Am. J. Hum. Genet. *93*, 915–925.
14. Gorden, N.T., Arts, H.H., Parisi, M.A., Coene, K.L., Letteboer, S.J., van Beersum, S.E., Mans, D.A., Hikida, A., Eckert, M., Knutzen, D., et al. (2008). CC2D2A is mutated in Joubert syndrome and interacts with the ciliopathy-associated basal body protein CEP290. Am. J. Hum. Genet. *83*, 559–571.
15. Garcia-Gonzalo, F.R., Corbit, K.C., Sirerol-Piquer, M.S., Ramaswami, G., Otto, E.A., Noriega, T.R., Seol, A.D., Robinson, J.F., Bennett, C.L., Josifova, D.J., et al. (2011). A transition zone complex regulates mammalian ciliogenesis and ciliary membrane composition. Nat. Genet. *43*, 776–784.
16. Ferland, R.J., Eyaid, W., Collura, R.V., Tully, L.D., Hill, R.S., Al-Nouri, D., Al-Rumayyan, A., Topcu, M., Gascon, G., Bodell, A., et al. (2004). Abnormal cerebellar development and axonal decussation due to mutations in AHI1 in Joubert syndrome. Nat. Genet. *36*, 1008–1013.
17. Edvardson, S., Shaag, A., Zenvirt, S., Erlich, Y., Hannon, G.J., Shanske, A.L., Gomori, J.M., Ekstein, J., and Elpeleg, O. (2010). Joubert syndrome 2 (JBTS2) in Ashkenazi Jews is associated with a TMEM216 mutation. Am. J. Hum. Genet. *86*, 93–97.
18. Davis, E.E., Zhang, Q., Liu, Q., Diplas, B.H., Davey, L.M., Hartley, J., Stoetzel, C., Szymanska, K., Ramaswami, G., Logan, C.V., et al.; NISC Comparative Sequencing Program (2011). TTC21B contributes both causal and modifying alleles across the ciliopathy spectrum. Nat. Genet. *43*, 189–196.
19. Dafinger, C., Liebau, M.C., Elsayed, S.M., Hellenbroich, Y., Boltshauser, E., Korenke, G.C., Fabretti, F., Janecke, A.R., Ebermann, I., Nürnberg, G., et al. (2011). Mutations in KIF7 link Joubert syndrome with Sonic Hedgehog signaling and microtubule dynamics. J. Clin. Invest. *121*, 2662–2667.
20. Coene, K.L., Roepman, R., Doherty, D., Afroze, B., Kroes, H.Y., Letteboer, S.J., Ngu, L.H., Budny, B., van Wijk, E., Gorden, N.T., et al. (2009). OFD1 is mutated in X-linked Joubert syndrome and interacts with LCA5-encoded lebercilin. Am. J. Hum. Genet. *85*, 465–481.
21. Cantagrel, V., Silhavy, J.L., Bielas, S.L., Swistun, D., Marsh, S.E., Bertrand, J.Y., Audollent, S., Attié-Bitach, T., Holden, K.R., Dobyns, W.B., et al.; International Joubert Syndrome Related Disorders Study Group (2008). Mutations in the cilia gene ARL13B lead to the classical form of Joubert syndrome. Am. J. Hum. Genet. *83*, 170–179.
22. Bielas, S.L., Silhavy, J.L., Brancati, F., Kisseleva, M.V., Al-Gazali, L., Sztriha, L., Bayoumi, R.A., Zaki, M.S., Abdel-Aleem, A., Rosti, R.O., et al. (2009). Mutations in INPP5E, encoding inositol polyphosphate-5-phosphatase E, link phosphatidyl inositol signaling to the ciliopathies. Nat. Genet. *41*, 1032–1036.
23. Baala, L., Romano, S., Khaddour, R., Saunier, S., Smith, U.M., Audollent, S., Ozilou, C., Faivre, L., Laurent, N., Foliguet, B., et al. (2007). The Meckel-Gruber syndrome gene, MKS3, is mutated in Joubert syndrome. Am. J. Hum. Genet. *80*, 186–194.
24. Arts, H.H., Doherty, D., van Beersum, S.E., Parisi, M.A., Letteboer, S.J., Gorden, N.T., Peters, T.A., Märker, T., Voesenek, K., Kartono, A., et al. (2007). Mutations in the gene encoding the basal body protein RPGRIP1L, a nephrocystin-4 interactor, cause Joubert syndrome. Nat. Genet. *39*, 882–888.
25. Badano, J.L., Mitsuma, N., Beales, P.L., and Katsanis, N. (2006). The ciliopathies: an emerging class of human genetic disorders. Annu. Rev. Genomics Hum. Genet. *7*, 125–148.
26. Dixon-Salazar, T., Silhavy, J.L., Marsh, S.E., Louie, C.M., Scott, L.C., Gururaj, A., Al-Gazali, L., Al-Tawari, A.A., Kayserili, H., Sztriha, L., and Gleeson, J.G. (2004). Mutations in the AHI1 gene, encoding jouberin, cause Joubert syndrome with cortical polymicrogyria. Am. J. Hum. Genet. *75*, 979–987.
27. Doherty, D. (2009). Joubert syndrome: insights into brain development, cilium biology, and complex disease. Semin. Pediatr. Neurol. *16*, 143–154.
28. Chávez, M., Ena, S., Van Sande, J., de Kerchove d'Exaerde, A., Schurmans, S., and Schiffmann, S.N. (2015). Modulation of ciliary phosphoinositide content regulates trafficking and Sonic Hedgehog signaling output. Dev. Cell *34*, 338–350.
29. Dyson, J.M., Conduit, S.E., Feeney, S.J., Hakim, S., DiTommaso, T., Fulcher, A.J., Sriratana, A., Ramm, G., Horan, K.A., Gurung, R., et al. (2017). INPP5E regulates phosphoinositide-dependent cilia transition zone function. J. Cell Biol. *216*, 247–263.
30. Garcia-Gonzalo, F.R., Phua, S.C., Roberson, E.C., Garcia, G., 3rd, Abedin, M., Schurmans, S., Inoue, T., and Reiter, J.F. (2015). Phosphoinositides regulate ciliary protein trafficking to modulate Hedgehog signaling. Dev. Cell *34*, 400–409.
31. He, M., Subramanian, R., Bangs, F., Omelchenko, T., Liem, K.F., Jr., Kapoor, T.M., and Anderson, K.V. (2014). The kinesin-4 protein Kif7 regulates mammalian Hedgehog signalling by organizing the cilium tip compartment. Nat. Cell Biol. *16*, 663–672.
32. Ko, H.W., Norman, R.X., Tran, J., Fuller, K.P., Fukuda, M., and Eggenschwiler, J.T. (2010). Broad-minded links cell cycle-related kinase to cilia assembly and hedgehog signal transduction. Dev. Cell *18*, 237–247.
33. Mariani, L.E., Bijlsma, M.F., Ivanova, A.I., Suciu, S.K., Kahn, R.A., and Caspary, T. (2016). Arl13b regulates Shh signaling from both inside and outside the cilium. Mol. Biol. Cell, mbc.E16-03-0189.
34. Qin, J., Lin, Y., Norman, R.X., Ko, H.W., and Eggenschwiler, J.T. (2011). Intraflagellar transport protein 122 antagonizes Sonic Hedgehog signaling and controls ciliary localization of pathway components. Proc. Natl. Acad. Sci. USA *108*, 1456–1461.
35. Clement, D.L., Mally, S., Stock, C., Lethan, M., Satir, P., Schwab, A., Pedersen, S.F., and Christensen, S.T. (2013). PDGFRα signaling in the primary cilium regulates NHE1-dependent fibroblast migration via coordinated differential activity of MEK1/2-ERK1/2-p90RSK and AKT signaling pathways. J. Cell Sci. *126*, 953–965.
36. Schneider, L., Clement, C.A., Teilmann, S.C., Pazour, G.J., Hoffmann, E.K., Satir, P., and Christensen, S.T. (2005).

PDGFRalphaalpha signaling is regulated through the primary cilium in fibroblasts. Curr. Biol. *15*, 1861–1866.

37. Bachmann-Gagescu, R., Dona, M., Hetterschijt, L., Tonnaer, E., Peters, T., de Vrieze, E., Mans, D.A., van Beersum, S.E., Phelps, I.G., Arts, H.H., et al. (2015). The ciliopathy protein CC2D2A associates with NINL and functions in RAB8-MICAL3-regulated vesicle trafficking. PLoS Genet. *11*, e1005575.
38. Bachmann-Gagescu, R., Phelps, I.G., Stearns, G., Link, B.A., Brockerhoff, S.E., Moens, C.B., and Doherty, D. (2011). The ciliopathy gene cc2d2a controls zebrafish photoreceptor outer segment development through a role in Rab8-dependent vesicle trafficking. Hum. Mol. Genet. *20*, 4041–4055.
39. Craige, B., Tsao, C.C., Diener, D.R., Hou, Y., Lechtreck, K.F., Rosenbaum, J.L., and Witman, G.B. (2010). CEP290 tethers flagellar transition zone microtubules to the membrane and regulates flagellar protein content. J. Cell Biol. *190*, 927–940.
40. Hoover, A.N., Wynkoop, A., Zeng, H., Jia, J., Niswander, L.A., and Liu, A. (2008). C2cd3 is required for cilia formation and Hedgehog signaling in mouse. Development *135*, 4049–4058.
41. Lancaster, M.A., Gopal, D.J., Kim, J., Saleem, S.N., Silhavy, J.L., Louie, C.M., Thacker, B.E., Williams, Y., Zaki, M.S., and Gleeson, J.G. (2011). Defective Wnt-dependent cerebellar midline fusion in a mouse model of Joubert syndrome. Nat. Med. *17*, 726–731.
42. Plotnikova, O.V., Seo, S., Cottle, D.L., Conduit, S., Hakim, S., Dyson, J.M., Mitchell, C.A., and Smyth, I.M. (2015). INPP5E interacts with AURKA, linking phosphoinositide signaling to primary cilium stability. J. Cell Sci. *128*, 364–372.
43. Singla, V., Romaguera-Ros, M., Garcia-Verdugo, J.M., and Reiter, J.F. (2010). Ofd1, a human disease gene, regulates the length and distal structure of centrioles. Dev. Cell *18*, 410–424.
44. Slaats, G.G., Saldivar, J.C., Bacal, J., Zeman, M.K., Kile, A.C., Hynes, A.M., Srivastava, S., Nazmutdinova, J., den Ouden, K., Zagers, M.S., et al. (2015). DNA replication stress underlies renal phenotypes in CEP290-associated Joubert syndrome. J. Clin. Invest. *125*, 3657–3666.
45. Ye, X., Zeng, H., Ning, G., Reiter, J.F., and Liu, A. (2014). C2cd3 is critical for centriolar distal appendage assembly and ciliary vesicle docking in mammals. Proc. Natl. Acad. Sci. USA *111*, 2164–2169.
46. O'Roak, B.J., Vives, L., Fu, W., Egertson, J.D., Stanaway, I.B., Phelps, I.G., Carvill, G., Kumar, A., Lee, C., Ankenman, K., et al. (2012). Multiplex targeted sequencing identifies recurrently mutated genes in autism spectrum disorders. Science *338*, 1619–1622.
47. Bachmann-Gagescu, R., Dempsey, J.C., Phelps, I.G., O'Roak, B.J., Knutzen, D.M., Rue, T.C., Ishak, G.E., Isabella, C.R., Gorden, N., Adkins, J., et al.; University of Washington Center for Mendelian Genomics (2015). Joubert syndrome: a model for untangling recessive disorders with extreme genetic heterogeneity. J. Med. Genet. *52*, 514–522.
48. Chong, J.X., Buckingham, K.J., Jhangiani, S.N., Boehm, C., Sobreira, N., Smith, J.D., Harrell, T.M., McMillin, M.J., Wiszniewski, W., Gambin, T., et al.; Centers for Mendelian Genomics (2015). The genetic basis of Mendelian phenotypes: discoveries, challenges, and opportunities. Am. J. Hum. Genet. *97*, 199–215.
49. Kircher, M., Witten, D.M., Jain, P., O'Roak, B.J., Cooper, G.M., and Shendure, J. (2014). A general framework for estimating the relative pathogenicity of human genetic variants. Nat. Genet. *46*, 310–315.
50. Paila, U., Chapman, B.A., Kirchner, R., and Quinlan, A.R. (2013). GEMINI: integrative exploration of genetic variation and genome annotations. PLoS Comput. Biol. *9*, e1003153.
51. Lek, M., Karczewski, K.J., Minikel, E.V., Samocha, K.E., Banks, E., Fennell, T., O'Donnell-Luria, A.H., Ware, J.S., Hill, A.J., Cummings, B.B., et al.; Exome Aggregation Consortium (2016). Analysis of protein-coding genetic variation in 60,706 humans. Nature *536*, 285–291.
52. Tennessen, J.A., Bigham, A.W., O'Connor, T.D., Fu, W., Kenny, E.E., Gravel, S., McGee, S., Do, R., Liu, X., Jun, G., et al.; Broad GO; Seattle GO; and NHLBI Exome Sequencing Project (2012). Evolution and functional impact of rare coding variation from deep sequencing of human exomes. Science *337*, 64–69.
53. Miller, J.A., Ding, S.L., Sunkin, S.M., Smith, K.A., Ng, L., Szafer, A., Ebbert, A., Riley, Z.L., Royall, J.J., Aiona, K., et al. (2014). Transcriptional landscape of the prenatal human brain. Nature *508*, 199–206.
54. GTEx Consortium (2013). The Genotype-Tissue Expression (GTEx) project. Nat. Genet. *45*, 580–585.
55. Alkuraya, F.S. (2010). Autozygome decoded. Genet. Med. *12*, 765–771.
56. Alkuraya, F.S. (2012). Discovery of rare homozygous mutations from studies of consanguineous pedigrees. Curr Protoc Hum Genet *Chapter 6*, Unit6 12.
57. Saudi Mendeliome Group (2015). Comprehensive gene panels provide advantages over clinical exome sequencing for Mendelian diseases. Genome Biol. *16*, 134.
58. Mefford, H.C., Yendle, S.C., Hsu, C., Cook, J., Geraghty, E., McMahon, J.M., Eeg-Olofsson, O., Sadleir, L.G., Gill, D., Ben-Zeev, B., et al. (2011). Rare copy number variants are an important cause of epileptic encephalopathies. Ann. Neurol. *70*, 974–985.
59. Kane, M.S., Davids, M., Bond, M.R., Adams, C.J., Grout, M.E., Phelps, I.G., O'Day, D.R., Dempsey, J.C., Li, X., Golas, G., et al. (2017). Abnormal glycosylation in Joubert syndrome type 10. Cilia *6*, 2.
60. Slaats, G.G., Isabella, C.R., Kroes, H.Y., Dempsey, J.C., Gremmels, H., Monroe, G.R., Phelps, I.G., Duran, K.J., Adkins, J., Kumar, S.A., et al. (2016). MKS1 regulates ciliary INPP5E levels in Joubert syndrome. J. Med. Genet. *53*, 62–72.
61. Stratigopoulos, G., Martin Carli, J.F., O'Day, D.R., Wang, L., Leduc, C.A., Lanzano, P., Chung, W.K., Rosenbaum, M., Egli, D., Doherty, D.A., and Leibel, R.L. (2014). Hypomorphism for RPGRIP1L, a ciliary gene vicinal to the FTO locus, causes increased adiposity in mice. Cell Metab. *19*, 767–779.
62. Westerfield, M. (1993). The zebrafish book: a guide for the laboratory use of zebrafish (*Brachydanio rerio*) (Eugene, OR: M. Westerfield).
63. Zou, J., Lathrop, K.L., Sun, M., and Wei, X. (2008). Intact retinal pigment epithelium maintained by Nok is essential for retinal epithelial polarity and cellular patterning in zebrafish. J. Neurosci. *28*, 13684–13695.
64. Hartmann, C., von Spiczak, S., Suls, A., Weckhuysen, S., Buyse, G., Vilain, C., Van Bogaert, P., De Jonghe, P., Cook, J., Muhle, H., et al. (2015). Investigating the genetic basis of fever-associated syndromic epilepsies using copy number variation analysis. Epilepsia *56*, e26–e32.

65. Mefford, H.C., Muhle, H., Ostertag, P., von Spiczak, S., Buysse, K., Baker, C., Franke, A., Malafosse, A., Genton, P., Thomas, P., et al. (2010). Genome-wide copy number variation in epilepsy: novel susceptibility loci in idiopathic generalized and focal epilepsies. PLoS Genet. *6*, e1000962.
66. Shaheen, R., Szymanska, K., Basu, B., Patel, N., Ewida, N., Faqeih, E., Al Hashem, A., Derar, N., Alsharif, H., Aldahmesh, M.A., et al.; Ciliopathy WorkingGroup (2016). Characterizing the morbid genome of ciliopathies. Genome Biol. *17*, 242.
67. Poretti, A., Huisman, T.A., Scheer, I., and Boltshauser, E. (2011). Joubert syndrome and related disorders: spectrum of neuroimaging findings in 75 patients. AJNR Am. J. Neuroradiol. *32*, 1459–1463.
68. Friede, R.L., and Boltshauser, E. (1978). Uncommon syndromes of cerebellar vermis aplasia. I: Joubert syndrome. Dev. Med. Child Neurol. *20*, 758–763.
69. Juric-Sekhar, G., Adkins, J., Doherty, D., and Hevner, R.F. (2012). Joubert syndrome: brain and spinal cord malformations in genotyped cases and implications for neurodevelopmental functions of primary cilia. Acta Neuropathol. *123*, 695–709.
70. Poretti, A., Brehmer, U., Scheer, I., Bernet, V., and Boltshauser, E. (2008). Prenatal and neonatal MR imaging findings in oral-facial-digital syndrome type VI. AJNR Am. J. Neuroradiol. *29*, 1090–1091.
71. Yachnis, A.T., and Rorke, L.B. (1999). Neuropathology of Joubert syndrome. J. Child Neurol. *14*, 655–659, discussion 669–672.
72. Romio, L., Fry, A.M., Winyard, P.J., Malcolm, S., Woolf, A.S., and Feather, S.A. (2004). OFD1 is a centrosomal/basal body protein expressed during mesenchymal-epithelial transition in human nephrogenesis. J. Am. Soc. Nephrol. *15*, 2556–2568.
73. Kobayashi, T., Kim, S., Lin, Y.C., Inoue, T., and Dynlacht, B.D. (2014). The CP110-interacting proteins Talpid3 and Cep290 play overlapping and distinct roles in cilia assembly. J. Cell Biol. *204*, 215–229.
74. Yin, Y., Bangs, F., Paton, I.R., Prescott, A., James, J., Davey, M.G., Whitley, P., Genikhovich, G., Technau, U., Burt, D.W., and Tickle, C. (2009). The Talpid3 gene (KIAA0586) encodes a centrosomal protein that is essential for primary cilia formation. Development *136*, 655–664.
75. Rosenbaum, J.L., Moulder, J.E., and Ringo, D.L. (1969). Flagellar elongation and shortening in Chlamydomonas. The use of cycloheximide and colchicine to study the synthesis and assembly of flagellar proteins. J. Cell Biol. *41*, 600–619.
76. Tamm, S.L. (1969). The effect of enucleation on flagellar regeneration in the protozoon *Peranema trichophorum*. J. Cell Sci. *4*, 171–178.
77. Chhin, B., Pham, J.T., El Zein, L., Kaiser, K., Merrot, O., and Bouvagnet, P. (2008). Identification of transcripts overexpressed during airway epithelium differentiation. Eur. Respir. J. *32*, 121–128.
78. Stolc, V., Samanta, M.P., Tongprasit, W., and Marshall, W.F. (2005). Genome-wide transcriptional analysis of flagellar regeneration in *Chlamydomonas reinhardtii* identifies orthologs of ciliary disease genes. Proc. Natl. Acad. Sci. USA *102*, 3703–3707.
79. Lefebvre, P.A., Nordstrom, S.A., Moulder, J.E., and Rosenbaum, J.L. (1978). Flagellar elongation and shortening in Chlamydomonas. IV. Effects of flagellar detachment, regeneration, and resorption on the induction of flagellar protein synthesis. J. Cell Biol. *78*, 8–27.
80. Ocbina, P.J., and Anderson, K.V. (2008). Intraflagellar transport, cilia, and mammalian Hedgehog signaling: analysis in mouse embryonic fibroblasts. Dev. Dyn. *237*, 2030–2038.
81. Grimes, D.T., Boswell, C.W., Morante, N.F., Henkelman, R.M., Burdine, R.D., and Ciruna, B. (2016). Zebrafish models of idiopathic scoliosis link cerebrospinal fluid flow defects to spine curvature. Science *352*, 1341–1344.
82. Vilboux, T., Doherty, D.A., Glass, I.A., Parisi, M.A., Phelps, I.G., Cullinane, A.R., Zein, W., Brooks, B.P., Heller, T., Soldatos, A., et al.; Nisc Comparative Sequencing Program (2017). Molecular genetic findings and clinical correlations in 100 patients with Joubert syndrome and related disorders prospectively evaluated at a single center. Genet. Med. Published online January 26, 2017. http://dx.doi.org/10.1038/gim.2016.204.
83. Keller, L.C., Romijn, E.P., Zamora, I., Yates, J.R., 3rd, and Marshall, W.F. (2005). Proteomic analysis of isolated chlamydomonas centrioles reveals orthologs of ciliary-disease genes. Curr. Biol. *15*, 1090–1098.
84. Mateja, A., Cierpicki, T., Paduch, M., Derewenda, Z.S., and Otlewski, J. (2006). The dimerization mechanism of LIS1 and its implication for proteins containing the LisH motif. J. Mol. Biol. *357*, 621–631.
85. Delto, C.F., Heisler, F.F., Kuper, J., Sander, B., Kneussel, M., and Schindelin, H. (2015). The LisH motif of muskelin is crucial for oligomerization and governs intracellular localization. Structure *23*, 364–373.
86. Ishikawa, H., Thompson, J., Yates, J.R., 3rd, and Marshall, W.F. (2012). Proteomic analysis of mammalian primary cilia. Curr. Biol. *22*, 414–419.
87. Mick, D.U., Rodrigues, R.B., Leib, R.D., Adams, C.M., Chien, A.S., Gygi, S.P., and Nachury, M.V. (2015). Proteomics of primary cilia by proximity labeling. Dev. Cell *35*, 497–512.
88. Li, J.B., Gerdes, J.M., Haycraft, C.J., Fan, Y., Teslovich, T.M., May-Simera, H., Li, H., Blacque, O.E., Li, L., Leitch, C.C., et al. (2004). Comparative genomics identifies a flagellar and basal body proteome that includes the BBS5 human disease gene. Cell *117*, 541–552.
89. Avidor-Reiss, T., Maer, A.M., Koundakjian, E., Polyanovsky, A., Keil, T., Subramaniam, S., and Zuker, C.S. (2004). Decoding cilia function: defining specialized genes required for compartmentalized cilia biogenesis. Cell *117*, 527–539.
90. Coordinators, N.R.; and NCBI Resource Coordinators (2016). Database resources of the National Center for Biotechnology Information. Nucleic Acids Res. *44* (D1), D7–D19.
91. Bae, Y.K., and Barr, M.M. (2008). Sensory roles of neuronal cilia: cilia development, morphogenesis, and function in *C. elegans*. Front. Biosci. *13*, 5959–5974.
92. Kunitomo, H., Uesugi, H., Kohara, Y., and Iino, Y. (2005). Identification of ciliated sensory neuron-expressed genes in *Caenorhabditis elegans* using targeted pull-down of poly(A) tails. Genome Biol. *6*, R17.
93. Vázquez-Manrique, R.P., González-Cabo, P., Ortiz-Martín, I., Ros, S., Baylis, H.A., and Palau, F. (2007). The frataxin-encoding operon of *Caenorhabditis elegans* shows complex structure and regulation. Genomics *89*, 392–401.
94. Lih, C.J., Cohen, S.N., Wang, C., and Lin-Chao, S. (1996). The platelet-derived growth factor alpha-receptor is encoded

by a growth-arrest-specific (gas) gene. Proc. Natl. Acad. Sci. USA *93*, 4617–4622.

95. Yeh, S.D., Chen, Y.J., Chang, A.C., Ray, R., She, B.R., Lee, W.S., Chiang, H.S., Cohen, S.N., and Lin-Chao, S. (2002). Isolation and properties of Gas8, a growth arrest-specific gene regulated during male gametogenesis to produce a protein associated with the sperm motility apparatus. J. Biol. Chem. *277*, 6311–6317.
96. Kim, Y.H., Epting, D., Slanchev, K., Engel, C., Walz, G., and Kramer-Zucker, A. (2013). A complex of BBS1 and NPHP7 is required for cilia motility in zebrafish. PLoS ONE *8*, e72549.
97. Sun, Z., Amsterdam, A., Pazour, G.J., Cole, D.G., Miller, M.S., and Hopkins, N. (2004). A genetic screen in zebrafish identifies cilia genes as a principal cause of cystic kidney. Development *131*, 4085–4093.
98. Lessieur, E.M., Fogerty, J., Gaivin, R.J., Song, P., and Perkins, B.D. (2017). The ciliopathy gene *ahi1* is required for zebrafish cone photoreceptor outer segment morphogenesis and survival. Invest. Ophthalmol. Vis. Sci. *58*, 448–460.
99. Krock, B.L., and Perkins, B.D. (2008). The intraflagellar transport protein IFT57 is required for cilia maintenance and regulates IFT-particle-kinesin-II dissociation in vertebrate photoreceptors. J. Cell Sci. *121*, 1907–1915.
100. Sukumaran, S., and Perkins, B.D. (2009). Early defects in photoreceptor outer segment morphogenesis in zebrafish ift57, ift88 and ift172 intraflagellar transport mutants. Vision Res. *49*, 479–489.

The American Journal of Human Genetics, Volume *101*

Supplemental Data

Mutations in *ARMC9*, which Encodes a Basal Body Protein, Cause Joubert Syndrome in Humans and Ciliopathy Phenotypes in Zebrafish

Julie C. Van De Weghe, Tamara D.S. Rusterholz, Brooke Latour, Megan E. Grout, Kimberly A. Aldinger, Ranad Shaheen, Jennifer C. Dempsey, Sateesh Maddirevula, Yong-Han H. Cheng, Ian G. Phelps, Matthias Gesemann, Himanshu Goel, Ohad S. Birk, Talal Alanzi, Rifaat Rawashdeh, Arif O. Khan, University of Washington Center for Mendelian Genomics, Michael J. Bamshad, Deborah A. Nickerson, Stephan C.F. Neuhauss, William B. Dobyns, Fowzan S. Alkuraya, Ronald Roepman, Ruxandra Bachmann-Gagescu, and Dan Doherty

Supplementary Data

Figure S1: zebrafish *armc9* gene structure and expression

(A) Schematic representation of the zebrafish *armc9* gene (with exonic/intronic structure) and protein below, showing the predicted LisH domain (green, N-terminal) and the armadillo-type-fold (ATF) domain (blue). **(B-K)** *In situ* hybridization on brain cryosections from adult zebrafish (**B-F** transverse sections, **G-K** sagittal sections). **(B)** Note staining along the ventricles marked with the arrows. **(C-E)** Higher magnification views of the boxed areas in **(B). (C)** Ventral zone of periventricular hypothalamus *Hv,* **(D)** periventricular grey zone of optic tectum *PGZ,* **(E)** lateral division of valvula cerebelli *Val* and torus longitudinalis *TL*. **(F)** Absence of staining with the control sense probe. **(G)** Sagittal section through the brain and eye, showing signal in the cerebellum (boxed area **H**), the hypothalamus (boxed area **I**) and the optic tectum (boxed area **J**). *CCe* corpus cerebelli, *LCa* lobus caudalis cerebelli, *H* periventricular hypothalamus, *PGZ* periventricular grey zone of optic tectum, *TL* torus longitudinalis. **(K)** Absence of staining with the control sense probe. Scale bars: 200µm (B,F,G,K), 50µm (C-E), 100 µm (H-J).

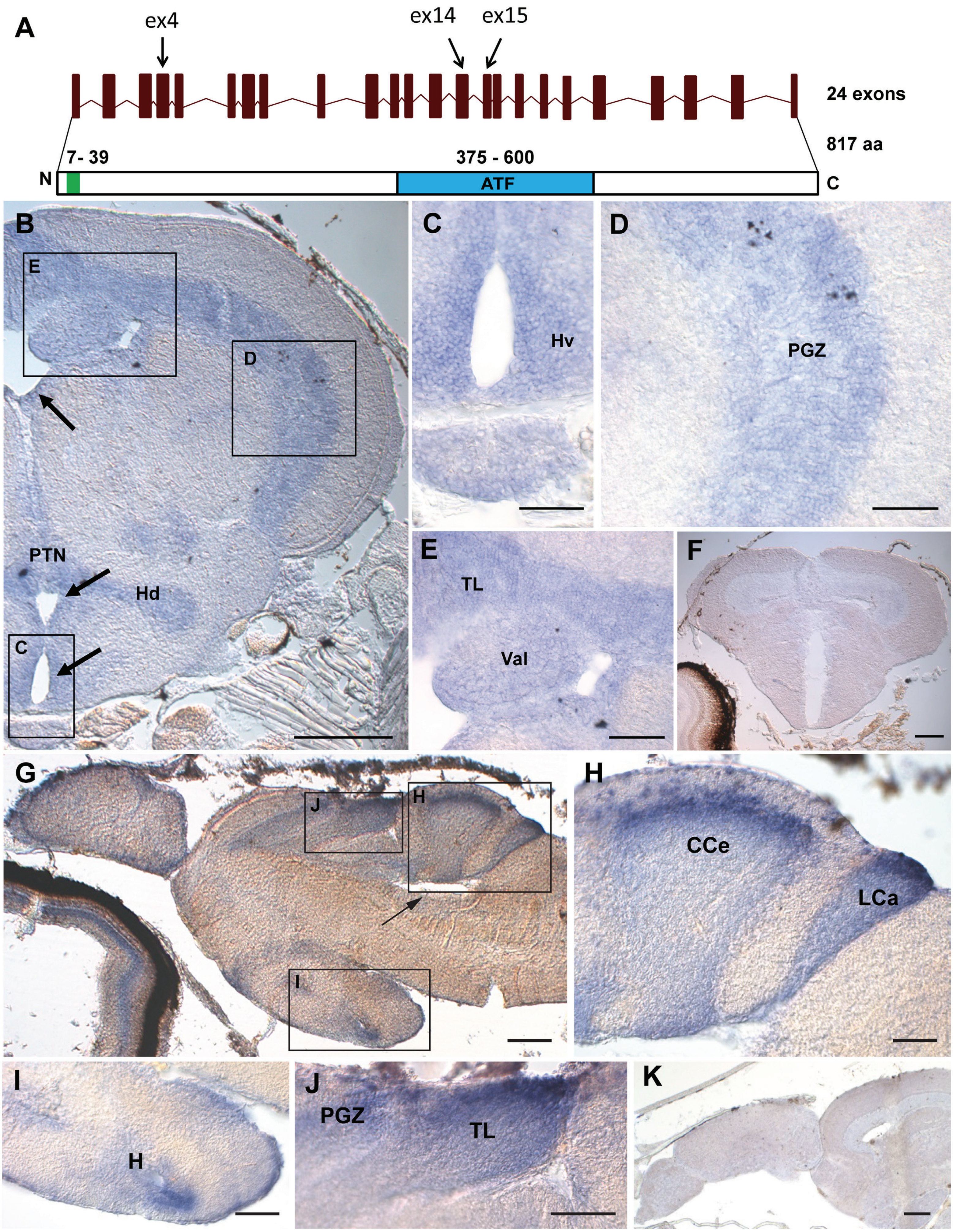
A
ex4
ex14
ex15
24 exons
817 aa
7- 39
375 - 600
N
ATF
C
B
E
D
PTN
Hd
C
C
Hv
D
PGZ
E
TL
Val
F
G
J
H
I
H
CCe
LCa
I
H
J
PGZ
TL
K

Fig S2: CRISPR/Cas9 *armc9* mutants

(A) Representative gel showing PCR amplification around the CRISPR target sites on finclips from adult F0 animals with body curvature. Note the presence of bands in addition to the WT-sized band in the curved fish. The PCR product from animal #2 was cloned and sequenced, revealing that 9 of 9 selected clones had small out-of-frame indels, indicating that this animal had a very high rate of mutations in *armc9* despite a wild-type-sized band on the gel. **(B-C)** Scanning electron microscopy (SEM) overview images of dissected and halved brains from F0 *armc9* animals with body curvature. The arrow points to the ventricular surfaces shown in **(D-E).** **(D-E)** Close up SEM images of the ventricular surface showing bundles of cilia in wild-type animals **(D)**. In contrast, *armc9* F0 mutant animals display a paucity of cilia **(E)**. **(F-I')** Immunohistochemistry on cryosections through whole eyes of wild-type **(F)** and an F0 *armc9* mutant **(G-I')** stained with the zpr1 antibody marking red-green cone cell bodies (red in **F-I**) and DiO highlighting photoreceptor (PR) outer segments (OS) (green in H-I). Note the thinner retinal layers and the coloboma (arrows in **G** and boxed area in **H**). **(I-I'')** represent the boxed area in **(H).** Note the discontinuity of the retinal layers and the presence of a second leaflet of retina folding back, with presence of PRs and OSs in a mirror image on either side of this aberrant second retinal layer (arrows). Scale bars are 100μm in (B-C), 3μm in (D-E), 100μm in (F-H), 50μm in (I'-I'').

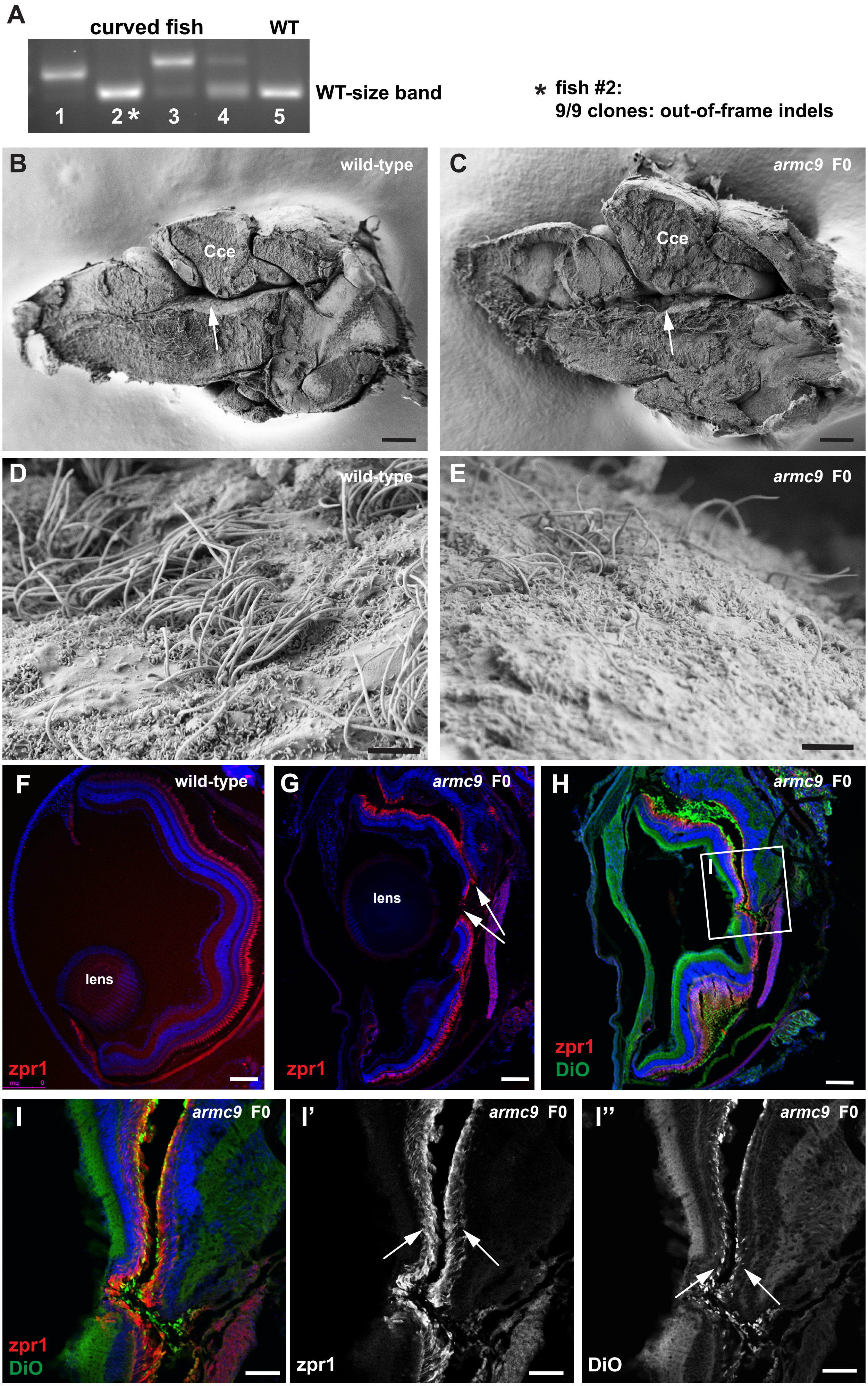
A
curved fish
WT
1
2 *
3
4
5
WT-size band
* fish #2:
9/9 clones: out-of-frame indels
B
wild-type
Cce
C
armc9 F0
Cce
D
wild-type
E
armc9 F0
F
wild-type
lens
zpr1
G
armc9 F0
lens
zpr1
H
armc9 F0
I
zpr1
DiO
I
armc9 F0
zpr1
DiO
I'
armc9 F0
zpr1
I''
armc9 F0
DiO

Fig S3: ARMC9 antibody validation

(A) Western blot analysis of hTERT-RPE cells transfected with non-targeting control siRNA and siARMC9. Cell lysates were probed with antibodies to ARMC9 and GAPDH as loading control.

(B) Quantification of western blot signal in (A) quantified via densitometry normalized to GAPDH.

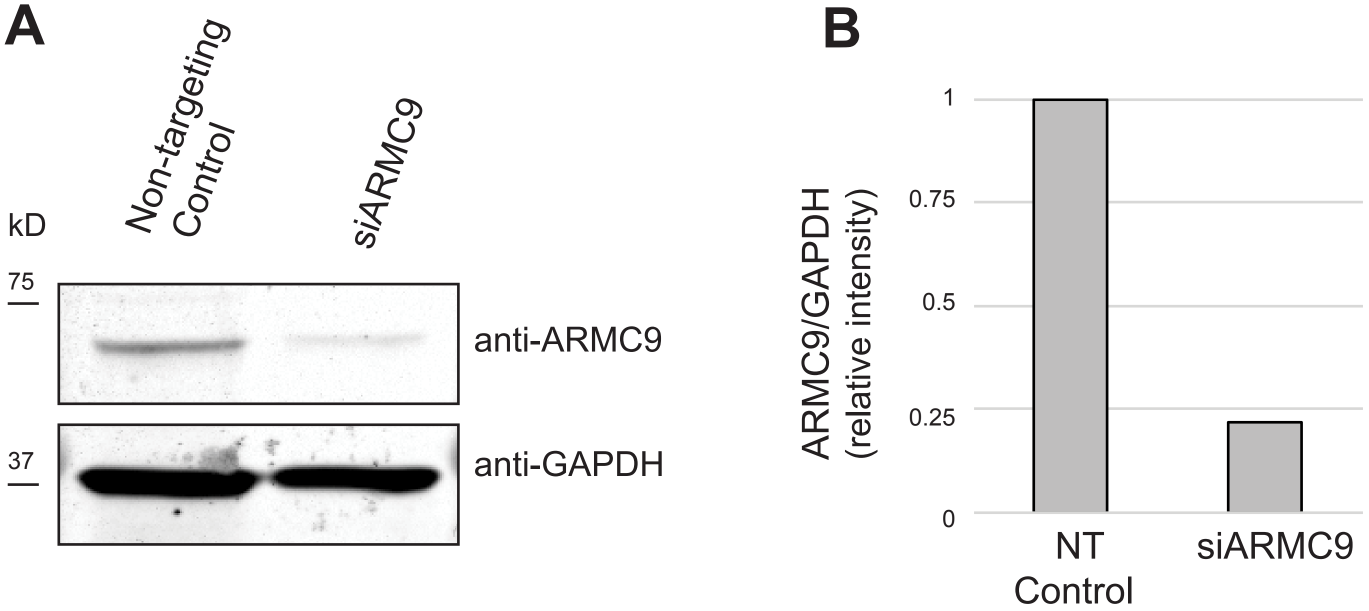
A
Non-targeting Control
siARMC9
kD
75
37
anti-ARMC9
anti-GAPDH
B
ARMC9/GAPDH (relative intensity)
1
0.75
0.5
0.25
0
NT Control
siARMC9

Table S1. Oligonucleotide primers for qPCR

Target Gene	**Primer ID**	**Sequence (5'-3')**
ARL13B Exons 2/3	Forward:	AATGCTGGTAAAACCGCAAC
	Reverse:	TTCCCCGAATTCTTATTCCA
ARMC9 Exons 21/22	Forward:	GGAGTGACCACCAGGGAATG
	Reverse:	GGCCACACGAAGAGAACAGA
ARMC9 Exons 3/4	Forward:	GAGACCGGACAAAGAGGAGC
	Reverse:	CTCTGTGGTCTGGCTCAAGG
ARMC9 Exons 2/3	Forward:	TTCCATCCGAGATGGGGACT
	Reverse:	GCTCCTCTTTGTCCGGTCTC
GAPDH Exons 2/6	Forward:	AGGTGAAGGTCGGAGTCAAC
		TTCACACCCATGACGAACAT

Table S2. Brain imaging findings in individuals with *ARMC9*-related Joubert syndrome

UW#	UW132-3	UW132-4	UW348-3	UW116-3	UW335-3	UW335-4	UW349-3	LR09-023	SA1-3	SA2-3	SA2-4
Age at MRI	29 yr	18 yr	10 mo	6 mo	2 mo	16 mo	7 mo	1 mo	14 mo	2 yr	4 yr
Molar Tooth Sign	Y	Y	Y	Y	Y	Y	Y	Y	Y	Y	Y
Agenesis of the corpus callosum	N	N	N	N	N	N	N	N	N	N	N
Ventriculomegaly	N	N	mild	mild	N	N	N	N	mild	N	N
PMG	N	N	N	N	N	N	N	N	N	N	N
Heterotopia	N	N	N	Y	N	Y	N	Y	N	N	N
Pituitary bright spot	P	P	P	P	P	P	A	P	A	P	P
Superior cb dysplasia	Y	Y	Y	Y	Y	Y	Y	Y	Y	Y	Y
cb hemisphere dysplasia	N	N	N	N	N	Y	N	Y	N	Y	N
cb atrophy	Y	Y	N	N	N	N	N	N	N	N	N
cervicomedulary heterotopia	N	N	unk	N	N	N	Y	possible	N	N	N
Foramen magnum cephalcele	unk	N	N	N	N	N	Y	possible	Y	N	N
		moderate-size retro-cb fluid		single L occipital PVNH		single L occipital PVNH	kinked brainstem	large posterior fossa with retro-cb fluid, single L temporal PVNH			thick corpus callosum

A=Absent, cb=cerebellar, L=Left, mo=months, N=No, P=Present, PMG=PolyMicroGyria, PVNH=PeriVentricular Nodular Heterotopia, unk=unknown, Y=Yes, yr=years,